Nickel-Platinum Nanoparticles as Peroxidase Mimics with a Record High Catalytic Efficiency

Zheng Xi,[†] Kecheng Wei,[§] Qingxiao Wang,[£] Moon J. Kim,[£] Shouheng Sun,[§] Victor Fung,[‡,*] and Xiaohu Xia[†,∥,*]

[†]Department of Chemistry and [∥]Nanoscience Technology Center, University of Central Florida, Orlando, Florida 32816, United States

[‡]Center for Nanophase Materials Sciences, Oak Ridge National Laboratory, Oak Ridge, Tennessee 37831, United States

[§]Department of Chemistry, Brown University, Providence, Rhode Island 02912, United States

[£]Department of Materials Science and Engineering, University of Texas at Dallas, Richardson, Texas 75080, United States

Supporting Information Placeholder

ABSTRACT: While nanoscale mimics of peroxidase have been extensively developed over the past decade or so, their catalytic efficiency as a key parameter has not been substantially improved in recent years. Herein, we report a class of highly efficient peroxidase mimic – nickel-platinum nanoparticles (Ni-Pt NPs) that consist of nickel-rich cores and platinum-rich shells. The Ni-Pt NPs exhibit a record high catalytic efficiency with a catalytic constant (K_{cat}) as high as 4.5×10^7 s^{-1}, which is about 46- and 10^4-fold greater than the K_{cat} values of conventional Pt nanoparticles and natural peroxidases, respectively. Density functional theory calculations reveal that the unique surface structure of Ni-Pt NPs weakens the adsorption of key intermediates during catalysis, which boosts the catalytic efficiency. The Ni-Pt NPs were applied to immunoassay of carcinoembryonic antigen that achieved an ultralow detection limit of 1.1 pg/mL, hundreds of times lower than that of the conventional enzyme-based assay.

Recently, enormous efforts have been devoted to developing peroxidase mimics (or artificial peroxidases) composed of inorganic nanostructures because of their emerging applications ranging from biosensing to imaging, therapy and environmental protection.[1-4] Compared with natural peroxidases, peroxidase mimics stand out due to their distinct advantages such as great stability, easy storage and facile production.[5,6] In this field, the bottleneck has been the limited catalytic efficiency of peroxidase mimics.[7,8] It should be emphasized that catalytic efficiency is a key parameter that largely determines the performance of peroxidase mimics in many applications because it measures the rate of signal generation.[8,9] The catalytic efficiencies, measured in terms of catalytic constant (K_{cat}, defined as the maximum number of products generated per second per catalyst),[10] for most known peroxidase mimics of 1-100 nm in dimensions are usually limited to the regime of 10^4-10^5 s^{-1}, which is only a few orders of magnitude greater than natural horseradish peroxidase (HRP) that serves as a benchmark (K_{cat} = 10^3 s^{-1}).[11-13] It is therefore imperative, though challenging, to break through such a limitation in catalytic efficiency.

Herein, we report a type of peroxidase mimic – nickel-platinum nanoparticles (Ni-Pt NPs) with Ni-rich cores and Pt-rich shells – which possesses a record high catalytic efficiency with K_{cat} of 10^7 s^{-1}. Notably, the Ni-Pt NPs were found to be much more efficient than pure Pt NPs (a well-known type of efficient peroxidase mimics[14,15]) with similar sizes. As a proof-of-concept demonstration, the Ni-Pt NPs were applied to a colorimetric immunoassay of carcinoembryonic antigen (CEA, a cancer biomarker[16]), which achieved an ultralow detection limit of 1.1 pg/mL, hundreds of times lower than that of a conventional HRP-based assay.

In a standard synthesis of Ni-Pt NPs, Ni(II) acetate and Pt(II) acetylacetonate with the same molar amounts were co-reduced by acetaldehyde in tetraethylene glycol (see Supporting Information, SI, for experimental details). Figure 1A shows a typical transmission electron microscopy (TEM) image of the Ni-Pt NPs. The size of Ni-Pt NPs was measured to be 13.9 ± 2.4 nm by randomly analyzing 200 particles (Figure S1). It is worth noting that this size is comparable to the size of an HRP molecule (4.03×6.75×11.71 nm in dimensions[17,18]). The atomic ratio of elemental Ni to Pt in the NPs was determined to be 49/51 (roughly 1:1) by inductively coupled plasma atomic emission spectroscopy (ICP-AES). Figure 1B shows a typical high-angle annular dark-field scanning TEM (HAADF-STEM) image of the Ni-Pt NPs, from which thin Pt-rich shells (with a brighter contrast[19]) on the surface of Ni-rich cores can be clearly resolved. The magnified atomic-resolution HAADF-STEM image taken from an individual NP (Figure 1C) indicates the existence of relatively dark spots in the Pt-rich shell, implying that a small portion of Ni atoms diffuse into Pt layers in the shell region.[20] This observation is consistent with the energy-dispersive X-ray spectroscopy (EDS) analyses (Figure 1D and 1E), where the core and shell of an individual NP were confirmed to be Ni-rich and Pt-rich, respectively. Figure S2 shows representative HAADF-STEM images of two additional Ni-Pt NP samples obtained from two different batches of synthesis. The overall particle sizes, morphologies, structures, as well as Ni/Pt ratios (determined by ICP-AES), of these samples were similar to the sample shown in Figure 1, indicating good reproducibility of the synthesis. The X-ray diffraction (XRD) pattern of the Ni-Pt NPs (Figure 1F) suggests the NPs take a face-centered cubic (*fcc*) structure, with the (111) diffraction peak resolved into two separate peaks that were probably caused by the Pt-rich shell (40.76°) and Ni-rich core (42.89°).[21] To understand the growth mechanism of Ni-Pt NPs with unique Ni-rich cores and Pt-rich shells, we monitored the growth of these NPs at different stages during the synthesis using TEM and ICP-AES (see Figure S3). Small nuclei of ~1 nm and Pt/Ni = 4:96 were observed at the initial stage (180 °C), suggesting the preferential reduction of Ni precursor. Thereafter, co-reduction of Ni and Pt precursors promoted the increase of particle size to ~11.5 nm (at 220 °C), where the Ni/Pt ratio was increased to 13:87. A core-shell structure could be observed when reaction temperature had been elevated to 240 °C. The particle size (*ca.* 14 nm) and Pt/Ni ratio (*ca.* 50:50) became stable after the temperature reached 280 °C.

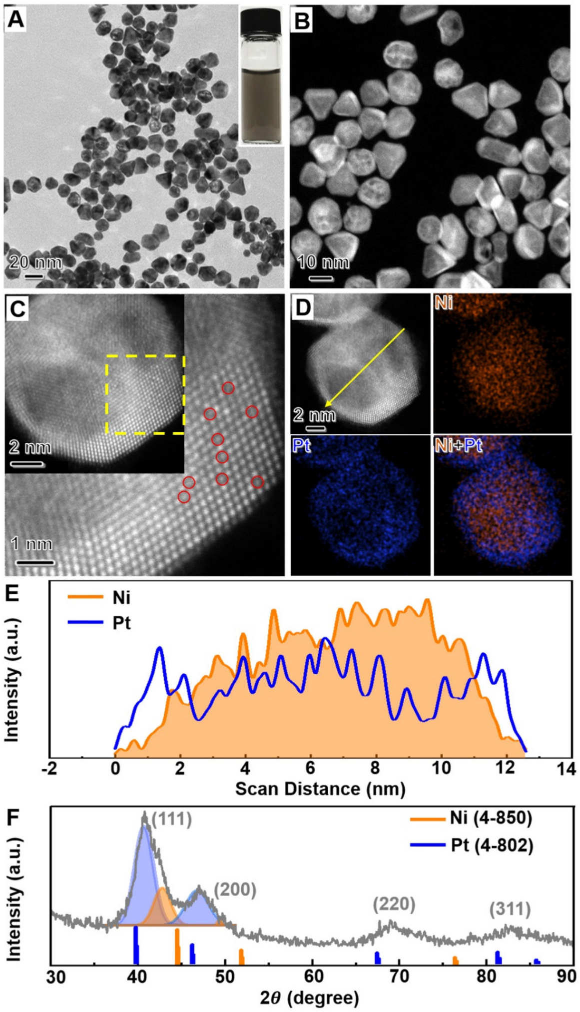

Figure 1. Structural and compositional analyses of Ni-Pt NPs. (A) TEM image, along with a photograph (inset) of the Ni-Pt NPs aqueous suspension; (B) HAADF-STEM image; (C) Atomic resolution HAADF-STEM image. Red circles highlight regions containing Ni atoms; (D) EDS mapping image, and (E) EDS line-scan that were recorded from an individual NP shown in (D) along the direction indicated by the arrow; (F) XRD pattern.

It should be emphasized that the NPs of different Ni/Pt atomic ratios could be obtained by simply varying the amounts of Ni and Pt precursors in a standard synthesis while keeping all other conditions unchanged. For example, NPs with Ni/Pt = 33/67 (Ni-Pt$_2$ NPs) and 62/38 (Ni-Pt$_{0.5}$ NPs) were obtained when the molar ratio of Ni and Pt precursors were changed from 1:1 in the standard synthesis to 1:2 and 2:1, respectively. If no Ni precursor was added to the synthesis, pure Pt NPs of ~14.6 ± 3.1 nm as final products were obtained (Figure S4). Those Ni-Pt$_2$ and Ni-Pt$_{0.5}$ NPs were carefully characterized by electron microscopes and XRD, and the results (Figures S5 and S6) demonstrated that: *i*) the sizes of Ni-Pt$_2$ and Ni-Pt$_{0.5}$ NPs were 12.7 ± 2.1 and 14.9 ± 2.2 nm, respectively; *ii*) both NPs had Ni-rich cores and Pt-rich shells, similar to that of Ni-Pt NPs; *iii*) Compared to Ni-Pt$_2$ NPs, the Ni-Pt$_{0.5}$ NPs had much thinner Pt-rich shells and higher Ni content on the surface. X-ray photoelectron spectroscopy (XPS) analysis (Figure S7) shows that Pt 4d and 4f peaks were clearly seen from all the three NPs of different Ni/Pt atomic ratios, while noticeable Ni signals could only be observed from Ni-Pt$_{0.5}$ NPs. High-resolution XPS spectra indicates that: Pt on the surface of all three NPs is primarily in the form of Pt(0) (Figure S8A);[22] and the content of Ni on the surface of Ni-Pt NPs decreases in the order of: Ni-Pt$_{0.5}$ NPs > Ni-Pt NPs > Ni-Pt$_2$ NPs (Figure S8B).[23] These XPS results are consistent with the HAADF-STEM and EDS data shown in Figures S5 and S6.

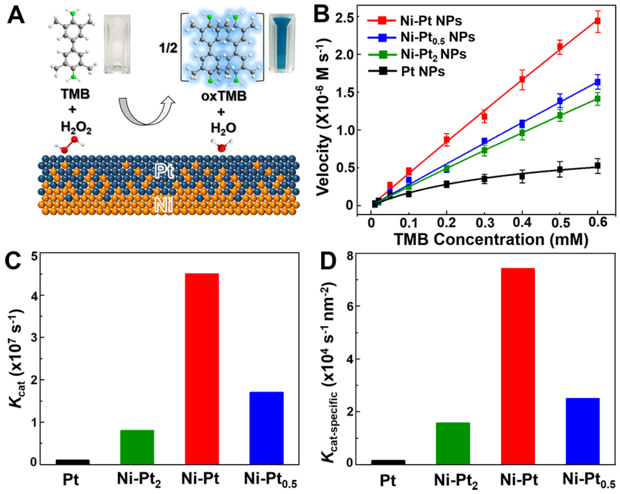

Figure 2. Peroxidase-like catalytic efficiencies of NPs with different Ni/Pt ratios. (A) Schematics showing the catalytic oxidation of TMB by H$_2$O$_2$; (B) Plots of initial reaction velocity for different NPs against TMB concentration. Error bars indicate standard deviations of three independent measurements; (C, D): histograms comparing K_{cat} (C) and $K_{cat\text{-}specific}$ (D) values of different NPs.

The peroxidase-like catalytic activities of the three types of NPs were evaluated through the oxidation of 3,3',5,5'-tetramethylbenzidine (TMB) by H$_2$O$_2$ as a model reaction.[9,13] This catalytic reaction yields a blue-colored product (*i.e.*, oxTMB with λ_{max} = 653 nm[24]) which can be conveniently monitored and quantified by a UV-vis spectrophotometer (Figure 2A). For comparison, the catalytic activity of pure Pt NPs (sample in Figure S4) was also determined. Apparent steady-state kinetic assays were performed to quantify their catalytic efficiencies (see the SI for details).[9,13] By plotting the initial reaction velocities against TMB concentration, typical Michaelis-Menten curves were observed (Figure 2B). These curves were then converted to the double double-reciprocal plots (Figure S9),[25] from which the K_{cat} values (Figure 2C) along with other kinetic parameters (Table S1) were derived. As shown by Figure 2C, K_{cat} values of the NPs displayed a volcano-shaped dependence on Ni contents, with the maximum point corresponding to Ni-Pt. Notably, the K_{cat} value of Ni-Pt NPs is as high as 4.5×10^7 s^{-1}, which is approximately 46- and 10^4-fold greater than those of Pt NPs ($K_{cat} = 9.7\times10^5$ s^{-1}) and HRP ($K_{cat} = 4.3\times10^3$ s^{-1})[9], respectively. Unlike HRP, all active atoms on the surface layers of a noble-metal peroxidase mimic contribute to its catalytic efficiency.[13,26,27] To better describe the catalytic efficiency of these NPs, we derived their area-specific efficiencies ($K_{\text{cat-specific}}$, the normalized K_{cat} to the surface area of an individual catalyst[8,28]). As shown by Figure 2D, a similar trend as K_{cat} was observed for the $K_{\text{cat-specific}}$. It is worth emphasizing that the Ni-Pt NPs exhibited a record-high catalytic efficiency, in terms of both K_{cat} and $K_{\text{cat-specific}}$, among all the already reported peroxidase mimics of 1-100 nm in dimension (see Table S2). As shown by Figure S10, no obvious changes of morphologies, structures and catalytic efficiencies of the Ni-Pt NPs were observed after they had been stored in deionized water at room temperature for 14 days, suggesting good stability of the NPs.

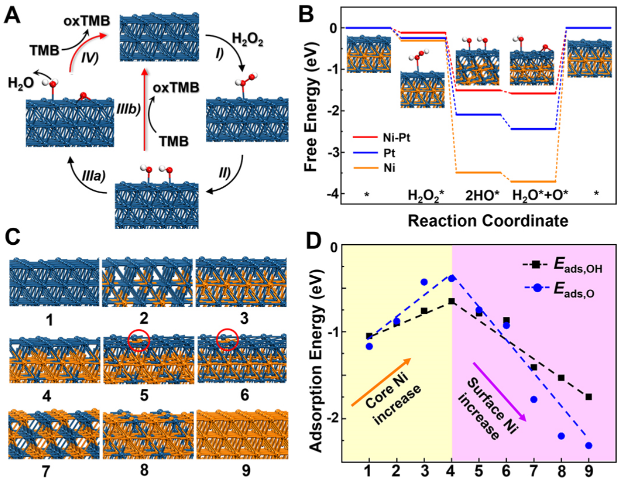

Figure 3. DFT calculations. (A) Proposed H_2O_2 decomposition pathway on Pt surface; (B) Free energy diagrams for H_2O_2 decomposition on Ni-Pt, Pt and Ni surfaces and optimized adsorption configurations on Ni-Pt surface; (C) Slab models for various NiPt surfaces (red circles highlight the single Ni atom on Pt top layer); (D) Adsorption energies for OH and O on the NiPt slab model surfaces in (C). Blue atoms represent Pt and orange atoms represent Ni in each slab model.

To elucidate the origin of the excellent peroxidase-like catalytic efficiency for the Ni-Pt NPs, we performed the density functional theory (DFT) calculations for H_2O_2 decomposition on different NiPt surfaces. Previous work postulated the H_2O_2 decomposition mechanism on metallic peroxidase mimic surface proceeds via $H_2O_2^* \rightarrow 2HO^* \rightarrow H_2O^* + O^*$, with the desorption of HO^*/O^* and oxidation of TMB to oxTMB as the key reaction steps (step IIIb and IV in Figure 3A).[29-31] Based on this, we first built three (111) slab models, including four-atomic layers of *i*) pure Pt, *ii*) pure Ni, and *iii*) one top Pt atomic layer plus three Ni/Pt 1/1 alloy layers, to simulate the Pt, Ni and Ni-Pt catalytic surfaces, respectively. The free energy diagram in Figure 3B compares the reaction steps on Pt, Ni and Ni-Pt surfaces with the corresponding intermediate adsorption configurations (Figure S11). The Ni-Pt surface has the weakest HO^*/O^* adsorption corresponding to a dramatic downshift of the *d*-band center of the Pt shell (Figure S12), indicating the most facile oxidant species transfer to the TMB substrate and thus is the most reactive peroxidase-like catalyst.[31] Moreover, to understand the volcano-type trend of the catalytic efficiency with the increase of Ni, we modeled the surfaces based on the characterizations showing the existence of Ni in the Pt surface layers and utilized the adsorption energies (E_{ads}) for OH and O as descriptors.[32] As demonstrated in Figure 3C and 3D, the same four-layer (111) slab models with a pure Pt top layer and an increasing Ni ratio from 0 to 0.75 (1~4 slab models in Figure 3C) in the following three sublayers based on the most stable bulk crystal structures for NiPt alloy compositions were used,[33,34] reflecting a larger Ni core and thinner Pt shell. The models used are similar to a previous theoretical study on the reactivity of Ni-containing Pt (111)-skin catalytic surfaces.[35] The $E_{\text{ads,OH}}$ and $E_{\text{ads,O}}$ increase monotonically from -1.05 eV (OH)/-1.17 eV (O) to -0.65 eV (OH)/-0.39 eV (O), suggesting that a thinner Pt shell on Ni core will have better peroxidase-like activity. However, if Ni atoms start to diffuse onto the top Pt surface layer, even single Ni atoms on the surface will lead to an obvious decrease of $E_{\text{ads,OH}}$ and $E_{\text{ads,O}}$ (5, 6 slab models compared with 4, 3 in Figure 3C) and thus lower the catalytic activity. With more Ni on the catalytic surface (7~9 slab models in Figure 3C), the activity will be further deteriorated. While we may not know the exact surface compositions for the catalysts, our models are sufficient to explain and predict the volcano-type activity trend with the increase of Ni component in such unique core-shell system, as the Ni-Pt maximizes the Ni core and Pt shell effect while avoiding too much Ni from leaching onto the Pt surface.

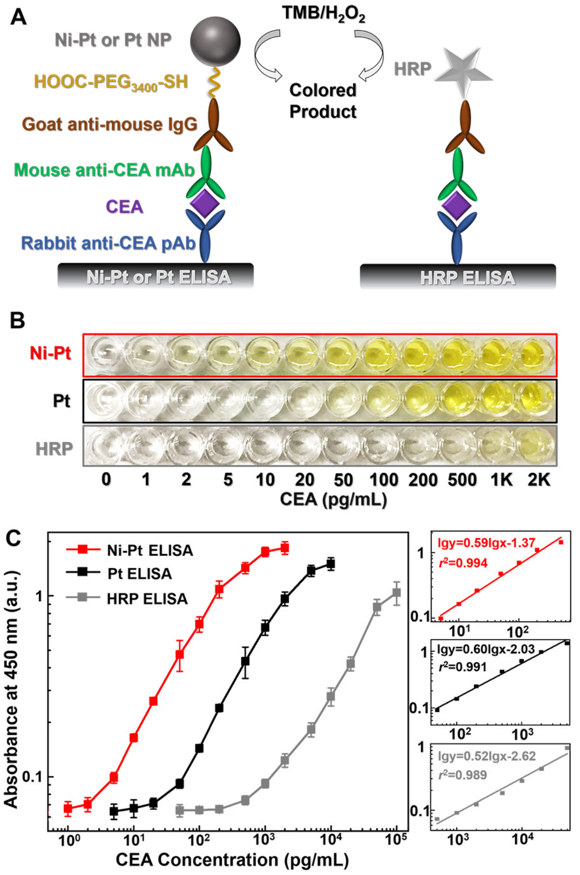

Figure 4. Detection of CEA with Ni-Pt NPs-, Pt NPs-, and HRP-based ELISAs. (A) Schematics of the three ELISAs of CEA; (B) Representative photographs taken from the ELISAs of CEA standards; (C) Corresponding calibration curves (left) along with linear range regions (right) of the detection results in (B). Error bars indicate standard deviations of eight independent measurements.

Finally, to demonstrate the potential application of the Ni-Pt NPs with maximized catalytic efficiency for biomedicine, a colorimetric enzyme-linked immunosorbent assay (ELISA) of carcinoembryonic antigen (CEA, a typical cancer biomarker[16]) was performed. For comparison, Pt NPs and HRP were also applied to the ELISA of CEA, where the same set of antibodies and materials were used. As shown by Figure 4A, the principle of Ni-Pt or Pt

ELISA is the same as conventional HRP ELISA,[36] except for the substitution of HRP with Ni-Pt or Pt NPs (see the SI for details). CEA standards of various concentrations were detected in a 96-well microtiter plate (Figure 4B). The absorbance of yellow-colored products (*i.e.*, diimine with λ_{max} = 450 nm that was converted from oxTMB[24]) in the wells was quantified using a plate reader. Figure 4C shows calibration curves of the ELISAs. The Ni-Pt ELISA displayed a quality linear detection range of 5-500 pg/mL, along with coefficients of variation in 1.3%-7.9%. The limit of detection (LOD, defined by the 3SD method[37]) of Ni-Pt ELISA was determined to be 1.1 pg/mL based on its calibration curve. In comparison, the LODs of Pt and HRP ELISAs were calculated to be 14.3 and 376 pg/mL, respectively, which are approximately 13- and 342-fold higher than that of Ni-Pt ELISA. Such a substantial enhancement in detection sensitivity for the Ni-Pt ELISA can be ascribed to the ultrahigh catalytic efficiency of the Ni-Pt NPs relative to Pt NPs and HRP because all other conditions of the three ELISAs were kept the same.

In summary, we have demonstrated a type of effective peroxidase mimics – Ni-Pt NPs that possess an ultrahigh catalytic efficiency with K_{cat} of 4.5×10^{7} s^{-1}. DFT calculations reveal that such an outstanding catalytic efficiency of Ni-Pt NPs is ascribed to their unique surface structure that weakens the adsorption of key intermediates during catalysis. The Ni-Pt NPs were applied to sensitive detection of CEA. The peroxidase mimics presented in this study may find widespread uses in biosensing, imaging and related fields.

ASSOCIATED CONTENT

Supporting Information

The Supporting Information is available free of charge on the ACS Publications website.

AUTHOR INFORMATION

Corresponding Author

Xiaohu Xia: Xiaohu.Xia@ucf.edu
Victor Fung: fungv@ornl.gov

Notes

The authors declare no competing financial interests.

ACKNOWLEDGMENT

This work was supported in part by the grants from the National Science Foundation (CHE-1834874 and CBET-1804525), the National Institute of Food and Agriculture, U.S. Department of Agriculture (2020-67021-31257), and the startup funds from University of Central Florida (UCF). M.J. Kim was supported in part by the Louis Beecherl, Jr. Endowment Funds.

REFERENCES

(1) Liu, B.; Sun, Z.; Huang, P.; Liu, J. Hydrogen Peroxide Displacing DNA from Nanoceria: Mechanism and Detection of Glucose in Serum. *J. Am. Chem. Soc.* **2015**, *137*, 1290-1295.

(2) Wang, W.; Jiang, X.; Chen, K. CePO$_4$: Tb, Gd Hollow Nanospheres as Peroxidase Mimic and Magnetic-Fluorescent Imaging Agent. *Chem. Commun.* **2012**, *48*, 6839-6841.

(3) Xu, B.; Wang, H.; Wang, W.; Gao, L.; Li, S.; Pan, X.; Wang, H.; Yang, H.; Meng, X.; Wu, Q.; Zheng, L.; Chen, S.; Shi, X.; Fan, K.; Yan, X.; Liu, H. A Single-Atom Nanozyme for Wound Disinfection Applications. *Angew. Chem. Int. Ed.* **2019**, *58*, 4911-4916.

(4) Herget, K.; Hubach, P.; Pusch, S.; Deglmann, P.; Gotz, H.; Gorelik, T. E.; Gural'skiy, I. A.; Pfitzner, F.; Link, T.; Schenk, S.; Panthofer, M.; Ksenofontov, V.; Kolb, U.; Opatz, T.; Andre, R.; Tremel, W. Haloperoxidase Mimicry by CeO$_{2-x}$ Nanorods Combats Biofouling. *Adv. Mater.* **2017**, *29*, 1603823.

(5) Wu, J.; Wang, X.; Wang, Q.; Lou, Z.; Li, S.; Zhu, Y.; Qin, L.; Wei, H. Nanomaterials with Enzyme-like Characteristics (Nanozymes): Next-Generation Artificial Anzymes (II). *Chem. Soc. Rev.* **2019**, *48*, 1004-1076.

(6) Jiang, D.; Ni, D.; Rosenkrans, Z. T.; Huang, P.; Yan, X.; Cai, W. Nanozyme: New Horizons for Responsive Biomedical Applications. *Chem. Soc. Rev.* **2019**, *48*, 3683-3704.

(7) Liang, M.; Yan, X. Nanozymes: From New Concepts, Mechanisms, and Standards to Applications. *Acc. Chem. Res.* **2019**, *52*, 2190-2200.

(8) Wei, Z.; Xi, Z.; Vlasov, S.; Ayala, J.; Xia, X. Nanocrystals of Platinum-Group Metals as Peroxidase Mimics for *in vitro* Diagnostics. *Chem. Commun.* **2020**, *56*, 14962-14975.

(9) Gao, L.; Zhuang, J.; Nie, L.; Zhang, J.; Zhang, Y.; Gu, N.; Wang, T.; Feng, J.; Yang, D.; Perrett, S.; Yan, X. Intrinsic Peroxidase-like Activity of Ferromagnetic Nanoparticles. *Nat. Nanotechnol.* **2007**, *2*, 577-583.

(10) Jiang, B.; Duan, D.; Gao, L.; Zhou, M.; Fan, K.; Tang, Y.; Xi, J.; Bi, Y.; Tong, Z.; Gao, G.; Xie, N.; Tang, A.; Nie, G.; Liang, M.; Yan, X. Standardized Assays for Determining the Catalytic Activity and Kinetics of Peroxidase-like Nanozymes. *Nat. Protoc.* **2018**, *13*, 1506-1520.

(11) Jin, S.; Wu, C.; Ye, Z.; Ying, Y. Designed Inorganic Nanomaterials for Intrinsic Peroxidase Mimics: A Review. *Sensor Actuat B-Chem* **2019**, 283, 18-34.

(12) Wang, Z.; Zhang, R.; Yan, X; Fan, K. Structure and Activity of Nanozymes: Inspirations for *de novo* Design of Nanozymes. *Mater. Today* **2020**, *41*, 81-119.

(13) Xia, X.; Zhang, J.; Lu, N.; Kim, M. J.; Ghale, K.; Xu, Y.; McKenzie, E.; Liu, J.; Ye, H. Pd-Ir Core-Shell Nanocubes: A Type of Highly Efficient and Versatile Peroxidase Mimic. *ACS Nano* **2015**, *9*, 9994-10004.

(14) Loynachan, C. N.; Thomas, M. R.; Gray, E. R.; Richards, D. A.; Kim, J.; Miller, B. S.; Brookes, J. C.; Agarwal, S.; Chudasama, V.; McKendry, R. A.; Stevens, M. M. Platinum Nanocatalyst Amplification: Redefining the Gold Standard for Lateral Flow Immunoassays with Ultrabroad Dynamic Range. *ACS Nano* **2018**, *12*, 279-288.

(15) Wu, R.; Chong, Y.; Fang, G.; Jiang, X.; Pan, Y.; Chen, C.; Yin, J.; Ge, C. Synthesis of Pt Hollow Nanodendrites with Enhanced Peroxidase-like Activity against Bacterial Infections: Implication for Wound Healing. *Adv. Funct. Mater.* **2018**, *28*, 1801484.

(16) Benchimol, S.; Fuks, A.; Jothy, S.; Beauchemin, N.; Shirota, K.; Stanners, C. P. Carcinoembryonic Antigen, a Human-Tumor Marker, Functions as an Intercellular-Adhesion Molecule. *Cell* **1989**, *57*, 327-334.

(17) Berglund, G. I.; Carlsson, G. H.; Smith, A. T.; Szoke, H.; Henriksen, A.; Hajdu, J. The Catalytic Pathway of Horseradish Peroxidase at High Resolution. *Nature* **2002**, *417*, 463-468.

(18) Gajhede, M.; Schuller, D. J.; Henriksen, A.; Smith, A. T.; Poulos, T. L. Crystal Structure of Horseradish Peroxidase C at 2.15 Angstrom Resolution. *Nat. Struct. Biol.* **1997**, *4*, 1032-1038.

(19) Cui, C.; Gan, L.; Heggen, M.; Rudi, S.; Strasser, P. Compositional Segregation in Shaped Pt Alloy Nanoparticles and Their Structural Behaviour during Electrocatalysis. *Nat. Mater.* **2013**, *12*, 765-771.

(20) Wang, L.; Gao, W.; Liu, Z.; Zeng, Z.; Liu, Y.; Giroux, M.; Chi, M.; Wang, G.; Greeley, J.; Pan, X.; Wang, C. Core-Shell Nanostructured Cobalt-Platinum Electrocatalysts with Enhanced Durability. *ACS Catal.* **2018**, *8*, 35-42.

(21) Zhang, S.; Hao, Y.; Su, D.; Doan-Nguyen, V. V.; Wu, Y.; Li, J.; Sun, S.; Murray, C. B. Monodisperse Core/Shell Ni/FePt Nanoparticles and Their Conversion to Ni/Pt to Catalyze Oxygen Reduction. *J. Am. Chem. Soc.* **2014**, *136*, 15921-15924.

(22) Arico, A. S.; Shukla, A. K.; Kim, H.; Park, S.; Min, M.; Antonucci, V. An XPS Study on Oxidation States of Pt and Its Alloys with Co and Cr and Its Relevance to Electroreduction of Oxygen. *Appl. Surf. Sci.* **2001**, *172*, 33-40.

(23) Biesinger, M. C.; Payne, B. P.; Grosvenor, A. P.; Lau, L. W. M.; Gerson, A. R.; Smart, R. S. Resolving Surface Chemical States in XPS Analysis of First Row Transition Metals, Oxides and Hydroxides: Cr, Mn, Fe, Co and Ni. *Appl. Surf. Sci.* **2011**, *257*, 2717-2730.

(24) Josephy, P. D.; Eling, T. E.; Mason, R. P. The Horseradish Peroxidase-Catalyzed Oxidation of 3,5,3',5'-Tetramethylbenzidine. Free Radical and Charge-Transfer Complex Intermediates. *J. Biol. Chem.* **1982**, *257*, 3669-3675.

(25) Lineweaver, H.; Burk, D. The Determination of Enzyme Dissociation Constants. *J. Am. Chem. Soc.* **1934**, *56*, 658-666.

(26) Xi, Z.; Cheng, X.; Gao, Z.; Wang, M.; Cai, T.; Muzzio, M.; Davidson, E.; Chen, O.; Jung, Y.; Sun, S.; Xu, Y.; Xia, X. Strain Effect in Palladium Nanostructures as Nanozymes. *Nano Lett.* **2020**, *20*, 272-277.

(27) Fang, G.; Li, W.; Shen, X.; Perez-Aguilar, J. M.; Chong, Y.; Gao, X.; Chai, Z.; Chen, C.; Ge, C.; Zhou, R. Differential Pd-Nanocrystal Facets Demonstrate Distinct Antibacterial Activity Against Gram-Positive and Gram-Negative Bacteria. *Nat. Commun.* **2018**, *9*, 129.

(28) Xi, Z.; Gao, W.; Xia, X. Size Effect in Pd-Ir Core-Shell Nanoparticles as Nanozymes. *ChemBioChem* **2020**, *21*, 2440-2444.

(29) Li, J.; Liu, W.; Wu, X. Gao, X. Mechanism of pH-switchable Peroxidase and Catalase-like Activities of Gold, Silver, Platinum and Palladium. *Biomaterials* **2015**, *48*, 37-44.

(30) Ge, C.; Fang, G.; Shen, X.; Chong, Y.; Wamer, W. G.; Gao, X.; Chai, Z.; Chen, C.; Yin, J. J. Facet Energy versus Enzyme-like Activities: The Unexpected Protection of Palladium Nanocrystals against Oxidative Damage. *ACS Nano* **2016**, *10*, 10436-10445.

(31) Wang, X.; Gao, X.; Qin, L.; Wang, C.; Song, L.; Zhou, Y.; Zhu, G.; Cao, W.; Lin, S.; Zhou, L.; Wang, K.; Zhang, H.; Jin, Z.; Wang, P.; Gao, X.; Wei, H. e_g Occupancy as an Effective Descriptor for the Catalytic Activity of Perovskite Oxide-based Peroxidase Mimics. *Nat. Commun.* **2019**, *10*, 704.

(32) Huang, L.; Chen, J.; Gan, L.; Wang, J.; Dong, S. Single-Atom Nanozymes. *Sci. Adv.* **2019**, *5*, eaav5490.

(33) Seo, O.; Lee, J. Y.; Kim, J. M.; Kim, J. W.; Kang, H. C.; Chung, J.; Noh, D. Y. Chemical Ordering in PtNi Nanocrystals. *J. Alloy Compd.* **2016**, *666*, 232-236.

(34) Paudyal, D.; Saha-Dasgupta, T.; Mookerjee, A. Study of Phase Stability in NiPt Systems. *J. Phys-Condens. Mat.* **2003**, *15*, 1029-1046.

(35) Su, H.; Bao, X.; Li, W. Modulating the Reactivity of Ni-Containing Pt(111)-Skin Catalysts by Density Functional Theory Calculations. *J. Chem. Phys.* **2008**, *128*, 194707.

(36) Lequin, R. M. Enzyme Immunoassay (EIA)/Enzyme-Linked Immunosorbent Assay (ELISA). *Clin. Chem.* **2005**, *51*, 2415-2418.

(37) Armbruster, D. A.; Tillman, M. D.; Hubbs, L. M. Limit of Detection (LQD)/Limit of Quantitation (LOQ): Comparison of the Empirical and the Statistical Methods Exemplified with GC-MS Assays of Abused Drugs. *Clin. Chem.* **1994**, *40*, 1233-1238.

TOC: